Journal of Computational Physics 228 (2009) 4200–4217

Contents lists available at ScienceDirect

Journal of Computational Physics

journal homepage: www.elsevier.com/locate/jcp

A high-order super-grid-scale absorbing layer and its application to linear hyperbolic systems

Daniel Appelö [*,1], Tim Colonius [1]

Division of Engineering and Applied Science, California Institute of Technology, 1200 E. California Boulevard, Pasadena, CA 91125, United States

ARTICLE INFO

Article history:
Received 19 September 2008
Received in revised form 17 February 2009
Accepted 19 February 2009
Available online 6 March 2009

MSC:
65M06
65M12
35L05
74J05
74S30

Keywords:
Absorbing layers
Non-reflecting boundary conditions
Perfectly matched layers
Maxwell's equations
Elastic waves

ABSTRACT

We continue the development of the super-grid-scale model initiated in [T. Colonius, H. Ran, A super-grid-scale model for simulating compressible flow on unbounded domains, J. Comput. Phys. 182 (1) (2002) 191–212] and consider its application to linear hyperbolic systems. The super-grid-scale model consists of two parts: reduction of an unbounded to a bounded domain by a smooth coordinate transformation and a damping of those scales. For linear problems the super-grid scales are analogous to spurious numerical waves. We damp these waves by high-order undivided differences. We compute reflection coefficients for different orders of the damping and find that significant improvements are obtained when high-order damping is used.

In numerical experiments with Maxwell's equations, we show that when the damping is of high order, the error from the boundary condition converges at the order of the interior scheme. We also demonstrate that the new method achieves perfectly matched layer-like accuracy.

When applied to linear hyperbolic systems the stability of the super-grid-scale method follows from its construction. This makes our method particularly suitable for problems for which perfectly matched layers are unstable. We present results for two such problems: elastic waves in anisotropic media and isotropic elastic waves in wave guides with traction-free surfaces.

1. Introduction

In the recent years there have been significant developments in the construction of accurate and efficient techniques to truncate unbounded domains encountered in applications in computational wave propagation, see, for example, the review articles [2–4]. The Maxwell system and the wave equation have proven popular for design of truncation techniques. The result is that for these equations there are excellent techniques available, particularly high-order local boundary conditions (HOLBCs) [5,6] and the perfectly matched layer (PML) [7]. Unfortunately, the generalization of these methods to other wave systems has not been completely successful. An important but negative stability result for the PML was established by Bécache et al. [8]. They found that the shape of the slowness curve for a given hyperbolic system determines whether or not a stable PML can be constructed. So far no equivalent result exists for HOLBCs but the recent results on the discrete equivalence between these and PML [2] indicate that the stability of HOLBCs could be similar to that of PML.

* Corresponding author.
E-mail addresses: appelo@caltech.edu (D. Appelö), colonius@caltech.edu (T. Colonius).
URLs: http://www.its.caltech.edu/~appelo (D. Appelö), http://www.colonius.caltech.edu (T. Colonius).

[1] This work was partially supported by the National Science Foundation (DMS-0514414).

0021-9991/$ - see front matter © 2009 Elsevier Inc. All rights reserved.
doi:10.1016/j.jcp.2009.02.030

Accuracy, stability and efficiency are the three key properties that must be taken into account in designing domain truncation techniques. For PML, accuracy is achieved by the "perfect matching" together with strong damping or wide layers. HOLBCs are constructed from sequences that converge to exact boundary conditions and thus become accurate if enough terms in the sequences are used. In the construction of both PML and HOLBCs, stability is secondary and has to be established for each application. This makes them less suitable for applications where the physical properties, models and governing equations change or are under development. Examples of such applications are seismic waves, aero acoustics, weather-prediction, atmospheric and climate modeling, ocean circulation, hydro acoustics and turbulence modeling.

In this paper we continue the development of the super-grid-scale (which we hereafter denote SuGS not to confuse it with sub-grid-stress) framework initiated in [1]. The SuGS model, originally developed for compressible flow, exploits the connection between coordinate mapping from bounded to unbounded domains and the filtering of the equations of motion to construct models that damp disturbances outside the near field. The two building blocks of the SuGS model are reduction of the unbounded domain (by windowing, coordinate transformation, grid stretching or slowing down of waves) and damping of the *super-grid* scales that cannot be represented on the bounded domain (the name, the super-grid-scale model, was chosen in [1] to convey the analogy with *sub-grid* modeling in large eddy simulations (LES)). In [1], where compressible flow was considered, the model used for the super-grid scales consisted of a parabolic damping term, motivated by an expansion of a product of filtered fields used in tensor diffusivity models for LES.

In this paper we focus on linear hyperbolic systems. As in [1] we reduce unbounded domains by a smooth coordinate transformation. The reduced problem consists of the original problem inside the *computational domain*, and a variable coefficient problem inside a *slowing-down* layer. Before discretization, the solutions inside the computational domain are identical. After discretization, the slowing down of waves causes an exponential (in time) decrease in the resolution of waves inside the layer. The result is that spurious numerical waves are reflected and pollute the solution in the computational domain. These super-grid scales are numerical and here we use high-order undivided differences to damp them. We find that when high-order accurate numerical methods are used inside the computational domain the use of a high-order undivided difference allows grid convergence at the rate of the interior scheme. In addition, as we start out with a hyperbolic system and add dissipation, it is easy to show that stability will be guaranteed.

The idea of coordinate transformation and damping is not new. Grosch and Orszag [9] studied pure grid-stretching and later dismissed it (in the words of [10]"It has been shown [9] that mapping by itself is doomed to fail for radiation problems..."). The high-order super-grid model we will present below can be seen as a generalization of the sponge layers studied by Israeli–Orzag [10] and Kosloff and Kossloff [11]. It is also an extension of Karni's slowing down and damping operator layer [12] and, Colonius and Ran's original super-grid-scale method [1] (when applied to linear problems). All these previous layers have been constructed with physical damping/dissipation in mind. However, as we will see below, if the damping is constructed with the discretized problem in mind, better results can be achieved. We note that an approach similar to the one discussed here has been used to construct non-reflecting boundary conditions by Visbal et al. for implicit compact schemes in [13,14].

2. One dimension

2.1. Grid stretching, slowing down of waves, converging characteristics and regularization of functions with steep gradients

Consider the transport equation

$$\begin{aligned} &\frac{\partial u}{\partial t} = a\frac{\partial u}{\partial x}, \quad -2 < x \leqslant 0, t > 0, a < 0, \\ &u(x,0) = u_0(x), \quad \text{supp } u_0 = x \in \Omega \equiv [-2,-1], \\ &u(-1,t) = 0. \end{aligned} \tag{1}$$

The solution of (1) is the right going wave $u(x,t) = u_0(at+x)$ which starts to exit the computational domain at time $t = 1/|a|$. The simplest possible non-reflecting boundary condition is to extend the computational domain by adding a layer in the right half plane, say to $x = L$. This allows for the simulation of waves inside the domain Ω up to time $(1+2L)/|a|$ without influence from the boundary. The drawback of this approach is that the size of the layer must be proportional to the desired final simulation time. Thus, if we intend to keep the computational efforts spent in the layer *fixed*, relative to those in the interior, as L increases; we need to keep the degrees of freedom of the discretized problem in the layer *fixed*.

In what follows it will be convenient to replace the constant coefficient equation (1) on the extended domain with an equivalent variable coefficient equation on a spatially fixed domain. To accomplish this the coordinate transformation $z = z(x)$, defined as the backwards solution from $x = L$ to $x = 0$ of the ordinary differential equation

$$\frac{dz(x)}{dx} = \eta(z(x),x), \quad z(L) = l \tag{2}$$

is used. With this coordinate transformation (1) reads

$$\frac{\partial u}{\partial t} = a\frac{dz}{dx}\frac{\partial u}{\partial z} = a\eta(z)\frac{\partial u}{\partial z}. \tag{3}$$

Our goal is to gradually slow down waves in the layer. Thus it is suitable to choose $\eta(z)$

$$\eta(z) = \begin{cases} 1, & z < 0, \\ \hat{\eta}, & \\ & 0 \leqslant z \leqslant l, \\ \varepsilon_L, & z = l. \end{cases}$$

In this paper we will for the most part use

$$\begin{aligned} &\hat{\eta}(z) = 1 - \sigma(z), \\ &\sigma(z) \equiv (1-\varepsilon_L)\left(1 - \left(1 - \frac{z}{l}\right)^p\right)^q. \end{aligned} \tag{4}$$

Note that $L \to \infty$ as $\varepsilon_L \to 0$, or vice versa. The smoothness of the mapping is determined by p and q, and should be chosen to match the order of accuracy of the numerical scheme.

From (3) it is clear that the residence time in the layer can be controlled by making L large or ε_L small. In the continuous setting, the procedure outlined above is an *exact* non-reflecting boundary condition up to a time determined only by L. However, after discretization the situation is different and unless care is taken, there will be significant spurious numerical reflections. The numerical difficulty arises when the wave speed in (3) tends to zero, as this causes the number of points per wavelength to approach zero.

Consider, for example, the case with $a = -1, \varepsilon_L = 0, q = 1, p = 1$ for $z \in [0, l]$ with $l = 1$, then (3) becomes

$$\begin{aligned} &\frac{\partial u}{\partial t} = -(1-z)\frac{\partial u}{\partial z}, \\ &u(z,0) = f(z). \end{aligned} \tag{5}$$

The characteristics of this equation are defined as the solutions of the ordinary differential equation

$$\frac{dz(t)}{dt} = -\eta(z)\Big|_{p=1,q=1} = -(1-z(t)). \tag{6}$$

For initial data $z(0) = z_0$ the solution is

$$z(t) - 1 = (z_0 - 1)e^{-t}, \tag{7}$$

or $z_0 = (z-1)e^t + 1$. Since we can solve (6) backward in time, for any point (z,t), there is a unique relation between z and t for any given z_0. Thus the solution to (5) is

$$u(z,t) = f(z_0) = f((z-1)e^t + 1). \tag{8}$$

The spatial derivatives of this function grow exponentially in time.

In Fig. 1 the characteristics for different values of p and q are plotted. As p and q increase, the characteristics converge faster. From Eq. (8) and Fig. 1 it can be seen that if, at some later time T, $f(z)$ should be resolved to the same degree as at

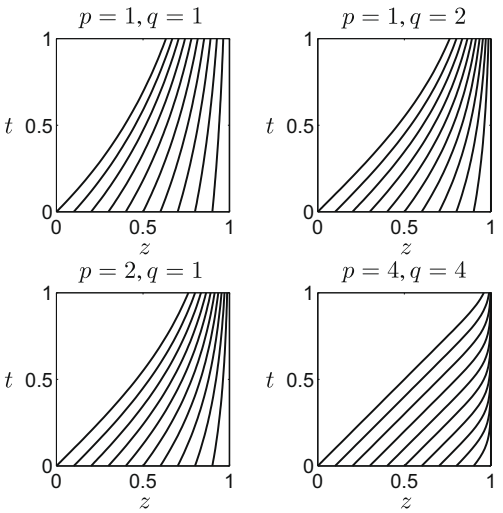

Fig. 1. Converging characteristics.

the initial time, then the number of degrees of freedom must increase exponentially. *This exponential loss of resolution is the principal cause for the reflections when (3) is used as a boundary condition.*

The phenomenon of spurious waves in finite-difference schemes, and their relations to the numerical dispersion relation are well understood and have been studied extensively [15–18]. In this setting, *spurious* is synonymous to *poorly resolved* and we therefore expect that direct application of the procedure above will suffer from severe pollution from backwards propagating spurious waves. In fact, if $\varepsilon_L \to 0$, and a centered finite-difference discretization is used, it can be seen (see, e.g. [17,18]) that the discrete energy of the incident wave will be conserved and reflected as spurious waves. We illustrate with an example.

2.2. A numerical example

To illustrate the typical numerical behavior for waves that are rapidly decelerated, we solve (3) with zero initial data on $z = [-1, l]$, with $l = 1/10$. The boundary condition is taken as $u(-1,t) = \sin(5\pi t)$ and we take $\varepsilon_L = 10^{-4}$. In space we discretize on a uniform grid with $h = 1/100$. We use a diagonal norm summation by parts operator (tabulated in Appendix C4 in [19]) that is fourth-order accurate on the boundary and eight-order accurate in the interior. The boundary condition is enforced using the simultaneous approximation technique, see e.g. [19]. To advance the solution in time, we use the classic fourth-order Adams–Bashforth method. The time step, $k = h/5$, is chosen based on the stability properties of the problem without the layer.

We advance the solution up to time 5. At this time the solution should be $u = \sin(5\pi(x-5))$, but as can be seen in Fig. 2(a) spurious waves have been created due to the spatially varying wave speed. If we try to refine the grid, the amplitude of the perturbation remains the same; only the frequency changes (they are ± 1 waves on the grid).

2.3. Regularization by artificial viscosity

The behavior of the solution as the characteristics converge is related to that of the development of discontinuous shock solutions in non-linear conservation laws (see, e.g. Chapter 8 in [20]). For problems with shocks, the most straightforward regularization is to add a suitable amount of artificial viscosity. Such regularization will remove spurious oscillations, but will also reduce the accuracy of the solution around the discontinuity and spoil the conservation. For the purpose of non-reflection and slowing down of waves considered here, the accuracy of solution inside the layer is of no importance as long as the errors do not exit the layer. We know that the discrete dispersion relation only supports backwards propagation out of the layer for waves that are highly under resolved; thus if such waves can be damped efficiently there should be little reflection.

To investigate the effect of regularization in our numerical example above we introduce artificial viscosity in the form of an undivided difference:

$$\frac{\partial u}{\partial t} = a\eta(z)\frac{\partial u}{\partial z} - \eta(z)\sum_{k\in K}(-1)^k h^{2k-1}\gamma_k \frac{\partial^k}{\partial z^k}\left(\sigma(z)\frac{\partial^k u}{\partial z^k}\right). \tag{9}$$

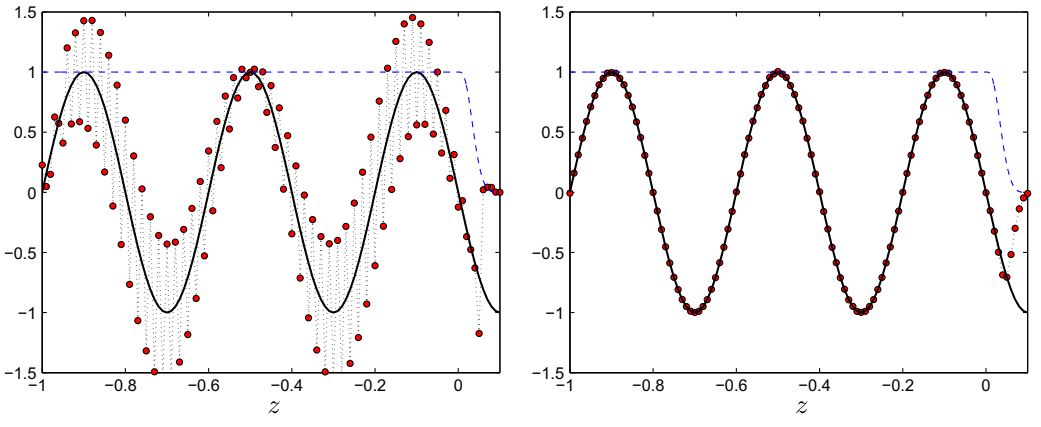

Fig. 2. To the left: spurious reflections due to slowing down of waves in the layer in $z \in [0, 0.1]$. To the right: A second-order damping term has been added in the layer and almost all oscillations have been removed and the exact and computed solution coincide. The blue line defines the slowing down function. Note that there are only ten grid points in the layer. (For interpretation of the references to colour in this figure legend, the reader is referred to the web version of this article.)

Here k is an element in a set of integers K. We say that the order of the damping term is $2k$ but note that the perturbation to the equation is actually $\mathcal{O}(h^{2k-1})$. The rationale of this scaling is that in the fully discretized problem, the size of the damping term will not depend on the time step or grid spacing. We can quickly determine the maximal allowable size on a coarse grid and then make the production run on a finer grid. Note that even though the coefficient of the damping term is small, $\mathcal{O}(h^{2k-1})$, the effect on plus–minus waves will be large. For the special case $\eta = \sigma = \gamma_k = 1$ each term in the sum will be of magnitude $h^{-1}2^{2k}$ when acting upon a $u_j = (-1)^j$, (again, the h^{-1} will be multiplied by Δt after time discretization is performed).

The effect of the added term is dramatic. For example, if the experiment above is repeated with $K = \{1\}$ and $\gamma_1 = 0.4$ significantly improved results, displayed in Fig. 2(b), are obtained. In one dimension there does not seem to be any benefit in using a higher-order damping, order 0 can be made as good as any other order if γ_0 is chosen to give maximal damping. In multiple dimensions, however, there is a substantial advantage in using higher-order damping terms as they cause a smaller impedance mismatch and less reflection. This will be demonstrated in Section 3.

2.4. Boundary conditions and well-posedness of the new model

Before discussing the above model in several dimensions we briefly address the well-posedness of Eq. (9) together with boundary conditions on the strip $z \in [-1, l]$. For simplicity we consider the problem

$$\begin{aligned} &\frac{\partial u}{\partial t} = -\eta(z)\frac{\partial u}{\partial z} - \eta(z)\tau_k \frac{\partial^k}{\partial z^k}\left(\sigma(z)\frac{\partial^k u}{\partial z^k}\right), \\ &u(z,0) = f(z) \in C^\infty(-1,l), \quad t \geqslant 0, z \in [-1,l]. \end{aligned} \tag{10}$$

Here $\tau_k = (-1)^k h^{2k-1}\gamma_k$ and k is an integer greater than or equal to one. It is assumed that $\eta(z), \sigma(z) \in C_0^\infty(-1,l)$, $\eta(z) \geqslant \eta_{min} > 0$ and that η goes to one and σ and its derivatives to zero at $z = -1$. The positivity of η allows us to define the scalar product and norm

$$(u,v)_\eta = \int_{-1}^{l} \frac{u(x)v(x)}{\eta(x)}dx, \quad \|u\|_\eta^2 \equiv (u,u)_\eta,$$

where u and v are real-valued functions.

The energy method applied to (10) gives:

$$\begin{aligned} \frac{1}{2}\frac{d}{dt}\|u\|_\eta^2 = (u,u_t)_\eta &= -\frac{1}{2}\left[u^2\right]_{-1}^{l} - \tau_k\left(u, \frac{\partial^k}{\partial z^k}\left(\sigma\frac{\partial^k u}{\partial z^k}\right)\right)_\eta \\ &= -\frac{1}{2}\left[u^2\right]_{-1}^{l} - \tau_k\left[u\frac{\partial^{k-1}}{\partial z^{k-1}}\left(\sigma\frac{\partial^k u}{\partial z^k}\right)\right]_{-1}^{l} + \tau_k\left(u_z, \frac{\partial^{k-1}}{\partial z^{k-1}}\left(\sigma\frac{\partial^k u}{\partial z^k}\right)\right)_\eta \\ &= -\frac{1}{2}\left[u^2\right]_{-1}^{l} - \tau_k\left[u\frac{\partial^{k-1}}{\partial z^{k-1}}\left(\sigma\frac{\partial^k u}{\partial z^k}\right)\right]_{-1}^{l} + \tau_k\left[u_z\frac{\partial^{k-2}}{\partial z^{k-2}}\left(\sigma\frac{\partial^k u}{\partial z^k}\right)\right]_{-1}^{l} \cdots - (-1)^k\tau_k\left\|\sqrt{\sigma}\frac{\partial^k u}{\partial z^k}\right\|_\eta. \end{aligned} \tag{11}$$

At the left boundary, all boundary terms except $u^2(-1)$ vanish along with the damping function σ. At the right boundary we must make all but the first term vanish, i.e. we must choose k boundary conditions from the pairs

$$u(l,t) = 0, \quad \frac{\partial^{k-1}}{\partial z^{k-1}}\left(\sigma\frac{\partial^k u}{\partial z^k}\right)(l,t) = 0, \tag{12}$$

$$u_z(l,t) = 0, \quad \frac{\partial^{k-2}}{\partial z^{k-2}}\left(\sigma\frac{\partial^k u}{\partial z^k}\right)(l,t) = 0, \tag{13}$$

$$\vdots$$

$$\frac{\partial^{k-1}u}{\partial z^{k-1}}(l,t) = 0, \quad \sigma\frac{\partial^k u}{\partial z^k}(l,t) = 0. \tag{14}$$

If both sides of (12) are used as boundary conditions, the right-hand side of (10) is still a semibounded operator. However, the resulting solution is not unique (the solution is over specified when $k+1$ boundary conditions are enforced). For the solution to be unique, the right-hand side of (10) should be a *maximal* semibounded operator. This will be the case if we choose precisely k boundary conditions from (12)–(14). We summarize this statement in the following corollary.

Corollary 1. *The initial-boundary value problem defined by Eq. (10) and the boundary condition $u(-1,t) = 0, t \geqslant 0$, together with k boundary conditions chosen from the k pairs (12)–(14), is well-posed. Moreover, the solution $u(z,t)$ is unique, as smooth as the initial data, and lies in the space of $C^\infty(-1,l)$ functions that satisfy the chosen combination of boundary conditions.*

Proof 1. The corollary follows from Theorem 7.8.1 in [21]. □

Remark 2. Note that when damping layers are added on both sides of the domain, it is convenient to make σ and η periodic and use periodic boundary conditions.

3. Multiple dimensions

The extension to d dimensions is straightforward. Let $u = u(x,t)$ be a n dimensional real-valued solution to the linear constant coefficient (strongly, strictly or symmetric) hyperbolic system

$$\frac{\partial u(x,t)}{\partial t} + \sum_{j=1}^{d} A_j \frac{\partial u(x,t)}{\partial x_j} = 0, \quad t \geqslant 0,\ x \in \mathbb{R}^d. \tag{15}$$

Assume that the initial data

$$u(x,0) = u_0(x)$$

are supported in the strip $-H < x_1 < -h$ and that we are only interested in simulating the solution in the half plane $x_1 < 0$. To truncate the domain we follow the one-dimensional procedure outlined in Section 2 and add a slowing-down layer and artificial viscosity:

$$\begin{aligned} &\frac{\partial u(x,t)}{\partial t} + \eta(x_1) A_1 \frac{\partial u(x,t)}{\partial x_1} + \sum_{j=2}^{d} A_j \frac{\partial u(x,t)}{\partial x_j} = -\eta(x_1) \sum_{k\in K} (-1)^k h^{2k-1} \gamma_k \frac{\partial^k}{\partial x_1^k}\left(\sigma(x_1)\frac{\partial^k u}{\partial x_1^k}\right), \\ &u(x,0) = u_0(x), \quad t \geqslant 0, x \in (-\infty, l) \times \mathbb{R}^{d-1}. \end{aligned} \tag{16}$$

Eq. (16) can be seen as a generalization of the sponge layers studied by Israeli–Orzag [10] (recovered with $\eta = 1$ and $K = \{0,2\}$), Kosloff and Kosslof's absorbing layer, [11], ($\eta = 1$ and $K = \{0\}$) Karni's slowing-down and damping operator layer [12] ($K = \{0\}$) and Colonius and Ran's super-grid-scale method ($K = \{1\}$), [1]. The model with pure stretching, studied, for example, by Grosch and Orszag, [9], is obtained by setting σ to zero.

A relevant question is whether there is a benefit of using the generalized model (16), rather than one of the previous models mentioned? If there is a benefit, it must arise due to the smaller magnitude of the coefficients in the higher-order damping terms. To investigate this, we compute the reflection coefficients for different choices of K.

3.1. Computed reflection coefficients

For one-dimensional problems with constant damping and stretching and with $K = 0, 1$, it is easy to write down the solutions inside and outside the layer and perform an analytic study of the reflection coefficient of a given layer. When the order of the damping operator increases, it becomes increasingly difficult to write down (manageable) closed from solutions in the layer. Hence, rather than perusing the (semi) analytic study of reflection coefficients pursued in [10–12] we adopt the ideas in [22], where direct simulations are used to compute reflection coefficients.

To compute the reflection coefficients for different K we solve the wave equation as a first-order system (15), defined by the matrices

$$A_1 = \begin{bmatrix} 0 & 1 & 0 \\ 1 & 0 & 0 \\ 0 & 0 & 0 \end{bmatrix}, \quad A_2 = \begin{bmatrix} 0 & 0 & 1 \\ 0 & 0 & 0 \\ 1 & 0 & 0 \end{bmatrix}, \quad u = \begin{bmatrix} p \\ u_1 \\ u_2 \end{bmatrix}.$$

Here p is the pressure and (u_1, u_2) are the velocities in the x and y directions (we use the notation $(x_1, x_2) = (x, y)$). The speed of sound is set to 1. We start the computation by placing the initial data

$$p(x,y,0) = \pi e^{-\frac{(x-x_s)^2+(y-y_s)^2}{\chi^2}}, \quad u_1(x,y,0) = u_2(x,y,0) = 0,$$

localized around a point (x_s, y_s) and record the pressure time histories in receiver points (x_r, y_r) along the dashed line in Fig. 3. Three setups, depicted in Fig. 3, are considered: (a) a domain with a damping layer in $0 < x \leqslant l$, (b) a domain with a solid wall at $x = 0$ and (c) a free space solution. For setups (a) and (b) the solution at the receivers can be decomposed as:

$$\begin{aligned} p_{\text{layer}}(x_r, y_r, t) &= p_{\text{free-space}}(x_r, y_r, t) + p_{\text{refl. layer}}(x_r, y_r, t), \\ p_{\text{solid}}(x_r, y_r, t) &= p_{\text{free-space}}(x_r, y_r, t) + p_{\text{refl. solid}}(x_r, y_r, t), \end{aligned}$$

where $p_{\text{free-space}}(x_r, y_r, t)$ is obtained from setup (c). At any point (x, y), $p_{\text{layer}}(x, y, t)$ and $p_{\text{solid}}(x, y, t)$ can be expressed in terms of its Fourier transform:

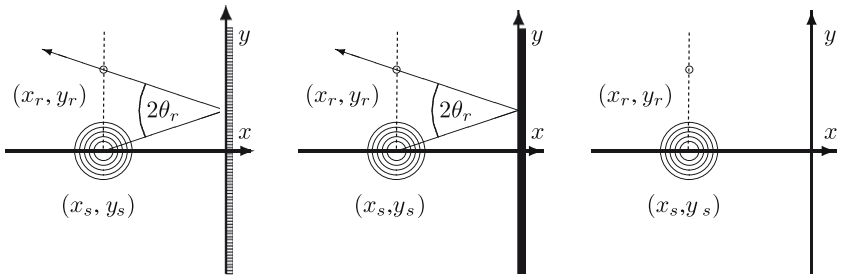

Fig. 3. Schematic pictures of the three cases.

$$\hat{p}_{\text{layer}}(x,y,f) = \int_{-\infty}^{\infty} e^{-i2\pi ft} p_{\text{layer}}(x,y,t)dt,$$
$$\hat{p}_{\text{solid}}(x,y,f) = \int_{-\infty}^{\infty} e^{-i2\pi ft} p_{\text{solid}}(x,y,t)dt.$$

This allows us to define the reflection coefficient

$$\hat{\mathcal{R}}(f,\theta_r) = \frac{\hat{p}_{\text{refl. layer}}(f,\theta_r)}{\hat{p}_{\text{refl. solid}}(f,\theta_r)}, \tag{17}$$

where θ_r is defined in Fig. 3.

Remark 3. Note that the solid wall case is only used to normalize the computation. An alternative is to send in planar waves at different angles but with the same amplitude, but this would require more than three computations.

3.1.1. Details of the computation

For all three setups we introduce a grid $(x_i, y_j) = (ih, jh)$ with $h = 1/200$ and place the initial data in $(x_s, y_s) = (-2, 0)$ with $\chi = 0.1$. The receivers recording the pressure time histories are placed in $(x_r, y_r) = (-2, vh)$, $v = 1, \ldots, 1600$. For all setups, periodic boundary conditions (placed sufficiently far away) are used in the y direction. For (c) we use periodic boundary conditions (placed sufficiently far away) in the x direction and for (b) we use symmetry conditions. For setup (a) a layer, $0 \leqslant x \leqslant 0.2$, is added (that is, 40 grid points in the layer). The layer is terminated by periodic boundary conditions. The spatial derivatives are approximated by 12th-order accurate, centered, finite-difference stencils and time integration is performed using the standard fourth-order accurate Runge–Kutta method. The solution is advanced up to time 30 (i.e. 8000 time steps) with a time step $\Delta t = 7/8h$. The damping and stretching are described by (4) with $\varepsilon_L = 10^{-4}$ and $p = q = 4$. We consider four layers: pure stretching, zero, second and eight-order damping. The maximal value of the damping, see Table 1, was chosen empirically by requiring the damped solutions to be stable in time with the same time step as the free-space problem.

In this example we use periodic boundary conditions so it is straightforward to discretize the damping terms, for $k = 0, 2, 4, \ldots$ we use:

$$\frac{\partial^k}{\partial x^k}\left(\sigma(x)\frac{\partial^k u}{\partial x^k}\right) \approx (D_+D_-)^{k/2}\sigma_i(D_+D_-)^{k/2}u_i, \tag{18}$$

and for $k = 1, 3, 5, \ldots$

$$\frac{\partial^k}{\partial x^k}\left(\sigma(x)\frac{\partial^k u}{\partial x^k}\right) \approx (D_+D_-)^{(k-1)/2}(D_+(\frac{\sigma_i + \sigma_{(i-1)/2}}{2})D_-)(D_+D_-)^{k-1}u_i. \tag{19}$$

For non-periodic domains it is customary to design the damping operators so that they are semi-definite by requiring that $(D_+)^k u_v = 0$ and $(D_-)^k u_v = 0$ in k grid points to the left and to the right of the first and final grid point. A thorough discussion of how to design semi-definite artificial viscosity operators can be found in [23].

Table 1
Damping coefficients used for the computation of reflection coefficients.

K	$\{\emptyset\}$	$\{0\}$	$\{1\}$	$\{4\}$
γ_k	0	500	1	0.01

3.1.2. Results

In Fig. 4 contours of $\log_{10}|\hat{\mathcal{R}}(f,\theta_r)|$ are plotted as a function of the frequency f and angle of incidence θ_r. In Fig. 4(a), the results for a pure stretching layer are plotted. It is clear that the poor results from the one-dimensional problem from Section 2.2 carry over to the two-dimensional setting. Indeed, the most significant reflection occurs for high frequency waves normal to the layer. The very large values of the reflection coefficient are a consequence of the transformation of well-resolved long-wavelength signals into short-wavelength spurious signals.

Fig. 4(b)–(d) show results for the damping layers of order zero, two and eight. In contrast to the pure stretching layer, the damped layers perform best for waves normal to the layer. The trend is clear, the higher the order of the damping, the smaller the mismatch in impedance, and the better the results. Note that for the highest angle of incidence there can be as many as four orders of magnitude difference in the reflection coefficient. This clearly demonstrates the improvement obtained using a high-order damping rather than the low-order damping used in classic layers. The improvement in non-reflectivity is due to the smaller mismatch, resulting from smaller coefficients in front of the damping term ($\sim 1, \sim h^1, \sim h^7$), in impedance between the computational domain and the layer.

Remark 4. In this experiment we discretized with a very high (12th) order spatial discretization to separate the filter error from the error of the interior scheme. In a realistic computation we would like (for optimal efficiency) to match the error from the boundary to the error from the interior scheme. Assuming the error in the interior is $\sim h^p$ we should either choose the filter of order p or $p+2$ as they have coefficients $\sim h^{p-1}$, $\sim h^{p+1}$. In Section 3.2.1 we try the first choice together with a high-order interior scheme and experience grid convergence on the order of the interior scheme (at least for moderate to long times). In Section 3.3.2 we try the second choice for a problem with a lower-order accurate interior scheme, for such cases it does seem to be beneficial to use a filter of order $p+2$.

Remark 5. Because we terminate the damping layers (for convenience) with periodic boundary conditions we make sure that no waves pass through the layer by monitoring the solution on the other side of the layer. With $\varepsilon_L = 10^{-4}$ only a very small fraction, insignificant for the computation of $\hat{\mathcal{R}}$, emerges on the other side.

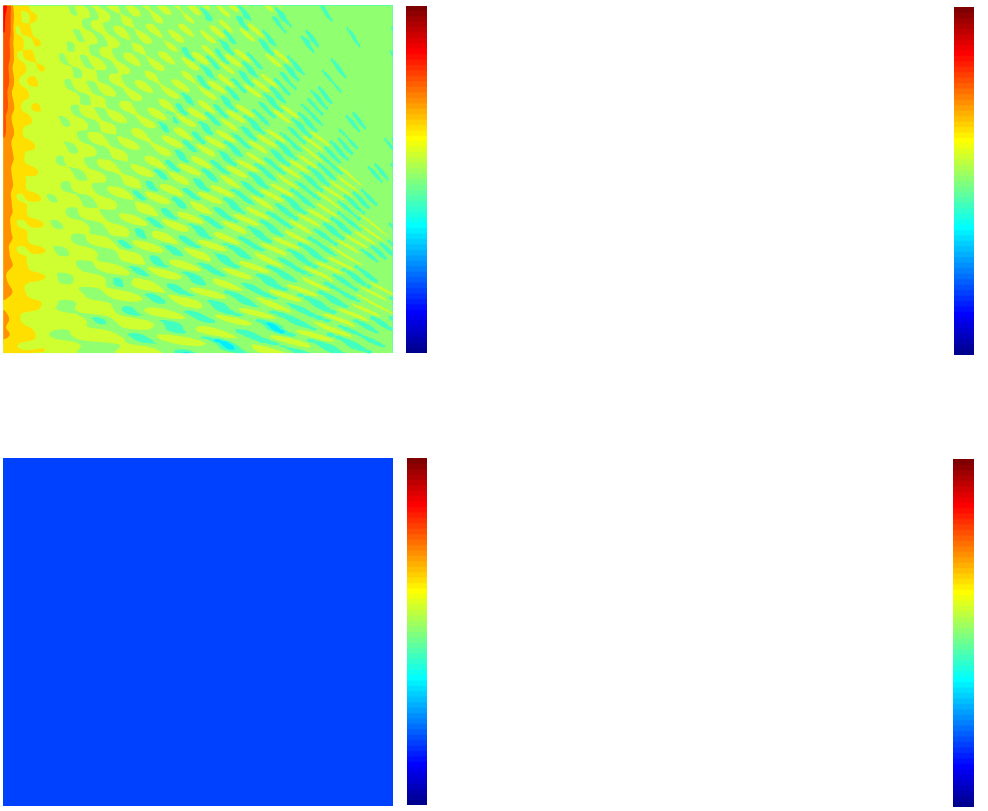

Remark 6. Finally, in this example we have used a 12th-order discretization in space, a fourth-order discretization in time and perturbed the equations by layers of order zero, two and eight by adding absorbing layers. As pointed out by one of the referees, the (relatively) low-order accuracy in time could potentially effect the results when the eight-order damping is used. That is, if a higher-order time discretization had been used the difference in performance between the eight-order layer and the other might have been even more striking.

3.2. Numerical study of grid convergence

In the previous section we showed results that indicate that the reflection of the proposed layer is reduced by using a higher-order damping. In this section we present numerical experiments with Maxwell's equations that demonstrate that grid convergence at the order of the interior method is obtained when a high-order damping is used in a thin, fixed-width, layer around the computational domain. We also demonstrate that the results compare well to those obtained with a PML.

3.2.1. Hagstrom's non-reflecting boundary condition problem

A challenging test problem for non-reflecting boundary conditions for the wave equation, Maxwell's equations, or the linearized Euler equations is the problem used by Hagstrom and coauthors in e.g. [24,25]. Here we use a version of the problem consisting of a rectangle occupying the domain $(x,y) \in [-2.1, 2.1] \times [0,1]$. The rectangle is periodic in y and open in the x direction. The task is to terminate the domain at $x = \pm 2.1$ with some non-reflecting boundary conditions. A schematic of the problem is depicted in Fig. 5. The exact solution is designed to contain large amounts of glancing and evanescent waves and is built up as a sum of y-periodic pulses:

$$u(x,y,t) = \sum_{k=-\infty}^{\infty} \int_{-\infty}^{t-r_k} \frac{e^{-95(t+0.5)^2}}{\sqrt{(t-s)^2) - r_k^2}} ds, \tag{20}$$

where $r_k^2 = x^2 + (y-k)^2$.

Here we choose to solve Maxwell's equation for the TE-mode (with the damping and slowing down added)

$$\begin{aligned}
\frac{\partial E_z}{\partial t} &= \eta \frac{\partial H_y}{\partial x} - \frac{\partial H_x}{\partial y} + \eta \left(\gamma_1 h \frac{\partial}{\partial x} \left(\sigma \frac{\partial E_z}{\partial x} \right) - \gamma_4 h^7 \frac{\partial^4}{\partial x^4} \left(\sigma \frac{\partial^4 E_z}{\partial x^4} \right) \right), \\
\frac{\partial H_x}{\partial t} &= -\frac{\partial E_z}{\partial y}, \\
\frac{\partial H_y}{\partial t} &= \eta \frac{\partial E_z}{\partial x} + \eta \left(\gamma_1 h \frac{\partial}{\partial x} \left(\sigma \frac{\partial H_y}{\partial x} \right) - \gamma_4 h^7 \frac{\partial^4}{\partial x^4} \left(\sigma \frac{\partial^4 H_y}{\partial x^4} \right) \right),
\end{aligned} \tag{21}$$

$$\begin{aligned}
&E_z(x,y,0) = E_z^0(x,y), \quad H_x(x,y,0) = H_x^0(x,y), \quad H_y(x,y,0) = H_y^0(x,y), \\
&-(2.1+l) \leqslant x \leqslant (2.1+l), 0 \geqslant y \geqslant 1, t \geqslant 0,
\end{aligned} \tag{22}$$

for which the exact solution, using (20), can be expressed as

$$E_z = \frac{\partial u}{\partial t}, \quad H_x = -\frac{\partial u}{\partial y}, \quad H_y = \frac{\partial u}{\partial x}.$$

As in Section 2 we can use the construction of the layer to establish well-posedness of the layer model. Let u and v be the real scalar functions defined on the domain defined in (22), and let $(v,u)_\eta$ and $\|u\|_\rho$ denote the weighted scalar product and norm

$$(u,v)_\rho = \int_{-(2.1+l)}^{(2.1+l)} \int_0^1 \frac{uv}{\rho} dy\, dx, (u,u)_\rho = \|u\|_\rho^2. \tag{23}$$

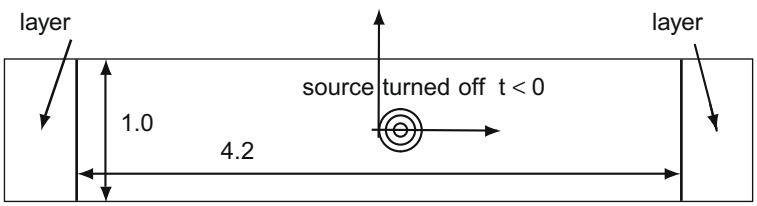

Fig. 5. Schematic picture of Hagstrom's problem. Note that the domain (and the initial data) is periodic in the y-direction so that the solution, at late times, mainly consists of glancing waves (the solution at time 20 is displayed in Fig. 9).

The following lemma is easily proved by use of the equations and integration by parts:

Lemma 1. *Assume $\eta \geqslant \eta_{min} > 0$ and $\sigma \geqslant 0$. Then the solution to (21) on the domain (22) with periodic boundary conditions in x and y satisfies the estimate*

$$\frac{1}{2}\frac{d}{dt}\left(\|E_z\|_\eta^2 + \|H_x\|_\eta^2 + \|H_y\|_\eta^2\right) = -\gamma_1 h\left\|\frac{\partial E_z}{\partial x}\right\|_{\sigma^{-1}}^2 - \gamma_1 h\left\|\frac{\partial H_y}{\partial x}\right\|_{\sigma^{-1}}^2 - \gamma_4 h^7\left\|\frac{\partial^4 E_z}{\partial x^4}\right\|_{\sigma^{-1}}^2 - \gamma_4 h^7\left\|\frac{\partial^4 H_y}{\partial x^4}\right\|_{\sigma^{-1}}^2. \tag{24}$$

3.2.2. Discretization and results

Eqs. (21) are discretized on the grid $(x_i, y_j) = (ih, jh), i = -N, \ldots, N, j = 0, \ldots, M, h = 1/M, 2.1 = hN$, with spatial derivatives approximated by the eight-order accurate stencil:

$$\frac{\partial u(x_i, y_j, t)}{\partial x} \approx D_0^x\left(1 - \frac{h^2}{6}D_+^x D_-^x + \frac{h^4}{30}(D_+^x D_-^x)^2 - \frac{h^6}{140}(D_+^x D_-^x)^3\right)u_{ij}(t).$$

The damping terms are approximated by (19) with $k = 1$ and (18) with $k = 4$. In time we discretize using an eight-order accurate Runge–Kutta method [26]. The unbounded direction, x, is truncated by adding layers in $|x| \leqslant 2.1 + l$ with damping functions

$$\eta(x) = 1 - \sigma(x),$$
$$\sigma(z) = \begin{cases} (1-\varepsilon_L)(1-(1-\frac{L-|x|}{l})^p)^q, & L < |x| < L + l, \\ 0, & |x| \leqslant L. \end{cases} \tag{25}$$

Here $L = 2.1$ and $p = q = 4$. In both directions the boundary conditions are taken to be periodic. In a first set of computations h is set to $h = 1/(25r), r = 2, 3, 6, 9$ and the layer width is fixed to $l = 0.6$. The damping is either second-order with $\gamma_1 = 5$ or eight-order with $\gamma_4 = 0.05$ (the values are chosen as the maximal values allowed by time stability without damping) and $\varepsilon_L = 10^{-4}$. The initial data and the exact solution at later times are computed using routines (described in [25]) generously supplied by Thomas Hagstrom. The solution is advanced up to time 100 and we measure the discrete L_2 error

$$e_2(t) = (h^2 \sum\sum (v_{ij}(t) - v^{exact}(x_i, y_j, t))^2)^{\frac{1}{2}}, \quad t = 2, 4, \ldots, 100.$$

Here $v = E_z, H_x, H_y$.

In Figs. 6 and 7 the errors for H_x and E_z are plotted as a function of time for the second- and eight-order damping. As can be seen from the dashed lines in Fig. 6 the results for the second-order damping appear to converge at a rate close to $h^{1/2}$ for both H_x and E_z. This rate is lower than expected (the damping term is a $\mathcal{O}(h)$ perturbation) and although there is convergence the error levels are large. A comparison of Fig. 6(a) and (b) reveals that there is no significant difference in the layers performance for E_z and H_x (the error for H_y is very similar to that of E_z and we limit our self to plot the latter only).

For the eight-order damping layer, the error of H_x is reduced as h^8 under grid refinement and, as can be seen in Fig. 7(a), the error only increases slightly over the duration of the simulation. The error in E_z also follows the h^8 trend, but only up to time ~ 40; then it starts to increase, see Fig. 7(b). There are two differences in the equation governing E_z and H_x, the stretching and the damping, which could explain the difference in error levels. When a damping term was added to the middle equation in (21) there was little, if any, change in the error levels of H_x and we therefore believe that the difference is caused

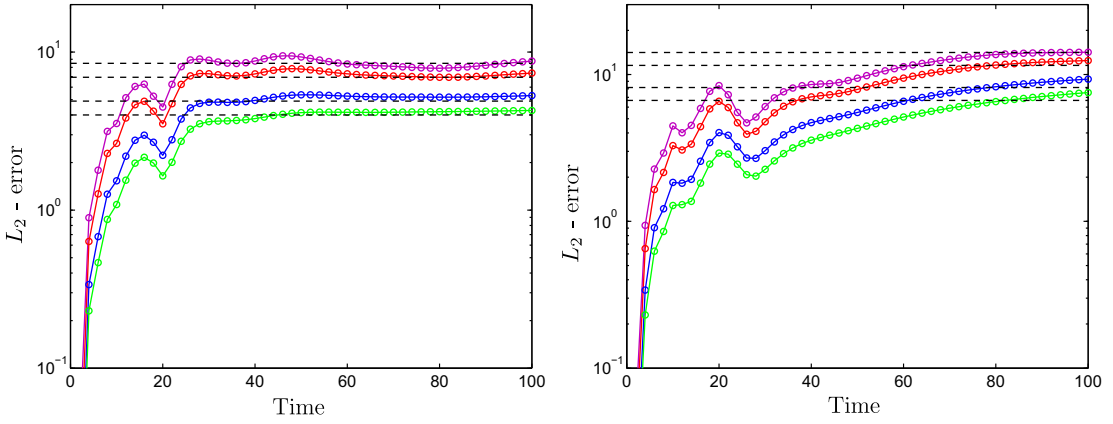

(a) L_2 error in H_x. (b) L_2 error in E_z.

Fig. 6. Errors for computations with second-order damping and $h = 1/(25r), r = 2, 3, 6, 9$. The dashed lines are $\sim h^{1/2}$ for different r.

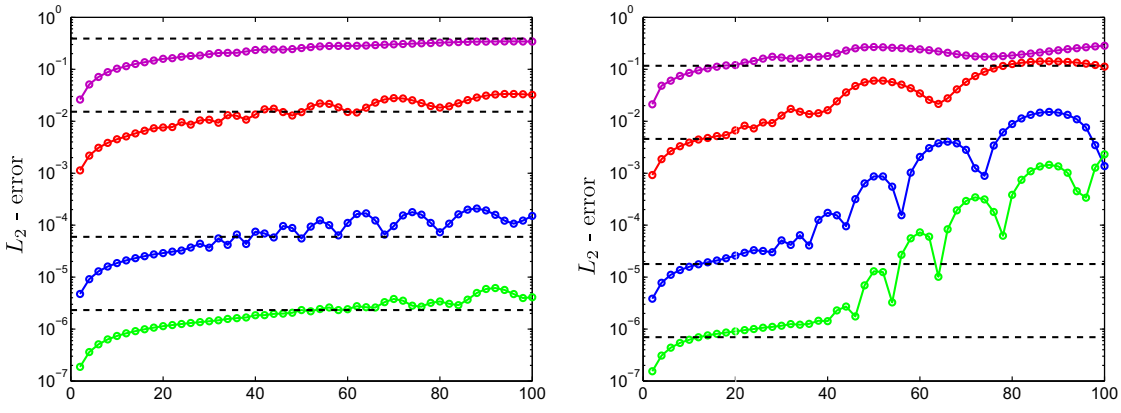

(a) L_2 error in H_x. (b) L_2 error in E_z.

Fig. 7. Errors for computations with eight-order damping and $h = 1/(25r), r = 2, 3, 6, 9$. The dashed lines are $\sim h^8$ for different r.

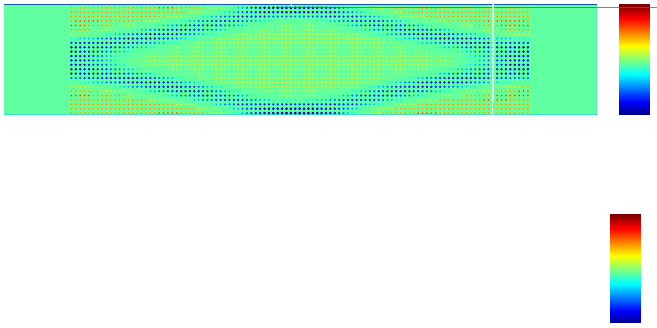

by the slowing down than by the damping. Fig. 8 shows the fact that the error appears to be of high frequency on the grid and also indicates that the slowing down generates more high frequency waves than can be damped. Nevertheless, the improvement in performance gained by the use of the eight-order damping is impressive. The difference in performance can be clearly seen in Figs. 8 and 9 where E_z and the error in E_z are plotted at time 20 for the two different damping terms.

We also study how the error behaves as the layer thickness changes. We fix $h = 1/(25 \cdot 6)$ and take the layer width $l = p \cdot 6h, p = 5, \ldots, 15$. The results for the second- and eight-order damping are plotted in Fig. 10(a) and (b), respectively. It is clear that the error decays very fast for the eight-order damping. It is also clear that unless the layer is wide enough, there can be a significant reduction in the performance of the layer. Presently we do not have a precise criterion to determine "how wide is wide enough"; however, it appears from simulations that the sufficient width decreases slightly (much slower than h^{-1}) as h is decreased. Therefore it is possible, but not convenient, to establish the sufficient layer width by a fast computation on a coarse grid.

3.2.3. Comparison with a perfectly matched layer

As a final test, we perform computations using a PML to truncate problem described in Section 3.2.1. The equations describing the PML are given in Appendix B.1. The values of the damping parameters in the PML have been optimized by linear sampling and the only remaining free parameter is the width of the PML.

In Fig. 11 we present comparisons between the error in E_z and H_x at two grid refinements for PML of width $l = 5/25, 7/25, 9/25$ and the eight-order damping layer, described above, width $l = 15/25$. The widths of the PML have been chosen such that the memory requirements do not supersede those of the damping layer (the PML requires 5/3 times the memory). In Fig. 11(a) it can be seen that for E_z the two thinner PMLs perform worse than the damping layer at early times and comparably or slightly better at late times. The widest PML performs about as well as the damping layer at early times and better at later times. The results for H_x are displayed in Fig. 11(b), here only the results of the widest PML are comparable to the damping layer.

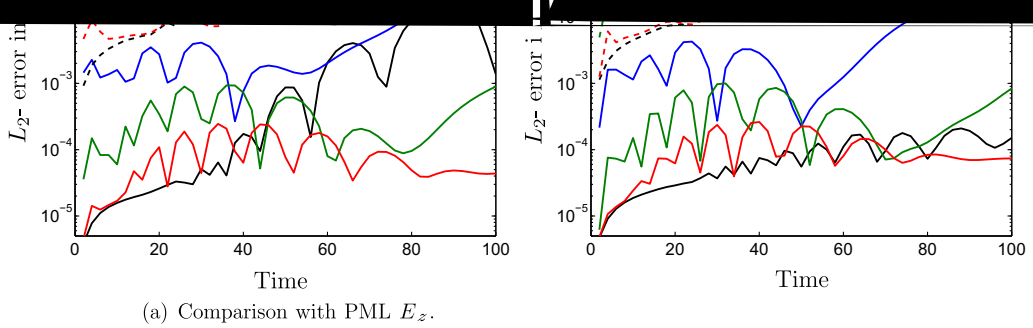

(a) Comparison with PML E_z.

From this single example it is not possible to make general conclusions about the relative accuracy and efficiency of the two layers, but the fact that the damping layer (in its simplicity) performs as well as the PML for this difficult problem suggests that further investigation of its use for Maxwell's equations is warranted.

3.3. Elastic waves

The results of the previous section are very encouraging, but the most significant benefits of the SuSG are expected for problems for which PML is unstable. In this section we demonstrate how the model can be used for two such problems: propagation of elastic waves in anisotropic media and in isotropic media with free surface boundary conditions.

3.3.1. Elastic waves in an anisotropic media: An example of blowup of PML and non-blowup for the super-grid-scale layer

The equations of motion in a continuum with no body forces can be written, with Einstein's summation convention,

$$\rho \frac{\partial^2 u_i}{\partial t^2} = \frac{\partial \sigma_{ij}}{\partial x_j}. \tag{26}$$

We work in two dimensions and therefore the indices i,j assume the values $\{1,2\}$. Here ρ is the density, u_1 and u_2 are the displacements and σ_{ij} is the stress tensor, which is related to the tensor of deformation

$$\varepsilon_{ij} = \frac{1}{2}\left(\frac{\partial u_i}{\partial x_j} + \frac{\partial u_j}{\partial x_i}\right),$$

by Hooke's law $\sigma_{ij} = c_{ijkl}\varepsilon_{kl}$, where c_{ijkl} is the tensor of elastic constants. Using the symmetry of the tensors σ_{ij}, ε_{kl} and c_{ijkl} and the scheme

$$(11) \leftrightarrow (1), \quad (22) \leftrightarrow (2), \quad (12) \leftrightarrow (21) \leftrightarrow (3),$$

which replaces two indices by one and four indices by two, we can write Hooke's law as $\sigma_n = c_{nm}\varepsilon_m, n, m = 1,2,3$, where $c_{mn} = c_{nm}$.

To simplify the comparison with PML for this problem we reformulate the second-order formulation (26) as a first-order system:

$$\frac{\partial v}{\partial t} = \begin{bmatrix} a_1^{11} & a_1^{12} \\ a_1^{21} & a_1^{2} \end{bmatrix} \frac{\partial v}{\partial x_1} + \begin{bmatrix} a_2^{11} & a_2^{12} \\ a_2^{21} & a_2^{2} \end{bmatrix} \frac{\partial v}{\partial x_2}, \quad a_1^{12} = \begin{bmatrix} \rho^{-1} & 0 & 0 \\ 0 & 0 & \rho^{-1} \end{bmatrix}, \quad a_2^{12} = \begin{bmatrix} 0 & 0 & \rho^{-1} \\ 0 & \rho^{-1} & 0 \end{bmatrix},$$
$$a_1^{21} = \begin{bmatrix} c_{11} & c_{13} \\ c_{12} & c_{23} \\ c_{13} & c_{33} \end{bmatrix}, \quad a_2^{21} = \begin{bmatrix} c_{13} & c_{12} \\ c_{23} & c_{22} \\ c_{33} & c_{23} \end{bmatrix}, \quad a_1^{11} = a_1^{22} = a_2^{11} = a_2^{22} = 0. \tag{27}$$

Here v_1, v_2 are the velocities and $v_3 = \sigma_1, v_4 = \sigma_2, v_5 = \sigma_3$, the stresses. We simplify the problem by considering an orthotropic media with principal axis coinciding with the x_1 and x_2 axes. For such media $c_{13} = c_{23} = 0$.

The stability of PML for the system (27) has been studied in [8,27]. In [8] necessary conditions on the coefficients c_{ij} for the stability of Berénger's split-field PML have been derived. By adding the so-called complex frequency shift it was possible to expand the parametric space of c_{ij} for which stable PML models can be constructed, see [27]. However, even with these improvements, there are still many medium for which PML cannot be used. Here we consider an "unstable" medium defined by the values $\rho = 1, c_{11} = 4, c_{22} = 20, c_{33} = 2, c_{12} = 7.5$.

To illustrate the stability properties of PML and the high-order super-grid-scale layer we solve (27) on the domain $(x_1, x_2) \in [-5,5]^2$ and truncate the domain in both x_1 and x_2 directions using either the perfectly matched layer given by Eq. (28) in [27] or the layer (16) with an eight-order damping term. A schematic description of the computational setup is found in Fig. 12(a).

The discretization is the same as in Section 3.2.1. The damping function in the PML is given by $\{d_1(x_1), d_2(x_2)\} = 10\sigma(z)$ where σ is the function (25) with $\varepsilon_L = 0, L = 5, l = 45h, p = q = 2$. The damping in the eight-order layer is also defined by (25), but with $\varepsilon_L = 10^{-4}, L = 5, l = 45h, p = q = 4$; the strength of the damping is $\gamma_4 = 0.04$. The grid spacing is $h = 10/405$ and the time step $\Delta t = 1/60$. The solution is advanced up to time 30 and started with the initial data:

$$v_1(x,y,0) = x_2 e^{-50((x_1+0.5)^2+(x_2-0.5)^2)},$$
$$v_2(x,y,0) = -x_1 e^{-50((x_1+0.5)^2+(x_2-0.5)^2)},$$
$$v_3 = v_4 = v_5 = 0.$$

In Fig. 13 the velocity in the x_1 direction, v_1, is plotted at different time instants. At first it appears that the PML absorbs all waves well, but around time 15 the solution starts to grow inside the PML, at time 20 (lower right in the figure) the instability begins to pollute the interior and at the end of the computation the solution has grown to 10^{12}. Contrary to the PML, the damping layer not only absorbs the waves efficiently, but also remains stable throughout the computation.

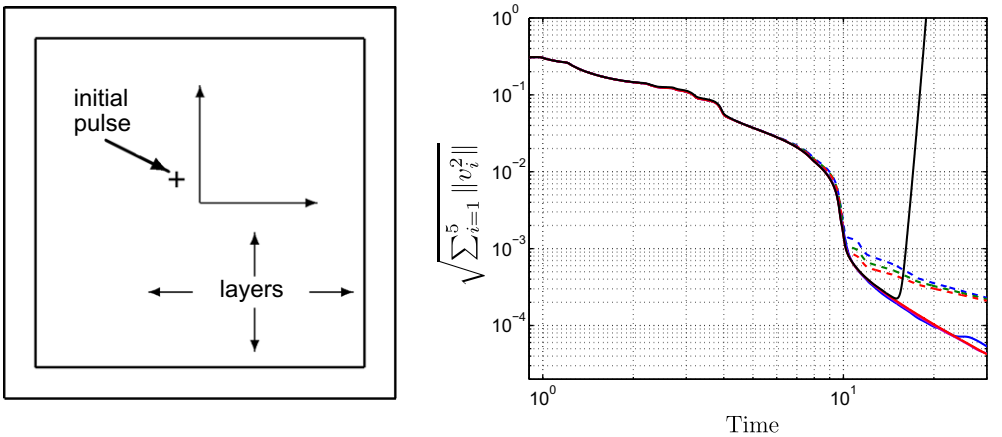

(a) Schematic setup. (b) Size of the solutions.

Fig. 12. To the left: schematic setup. To the right: Square root of the sum of the squares of the l_2 norm of $v_i, i = 1, \ldots, 5$, as a function of time for the PML layer and the super-grid-scale layer. The black line is the PML, the dashed lines are for second-order damping and the solid for eight-order damping. The blue, green and red are for refinements $h = 10/(135r), r = 3, 4, 5$. The PML computation uses $r = 3$. (For interpretation of the references to colour in this figure legend, the reader is referred to the web version of this article.)

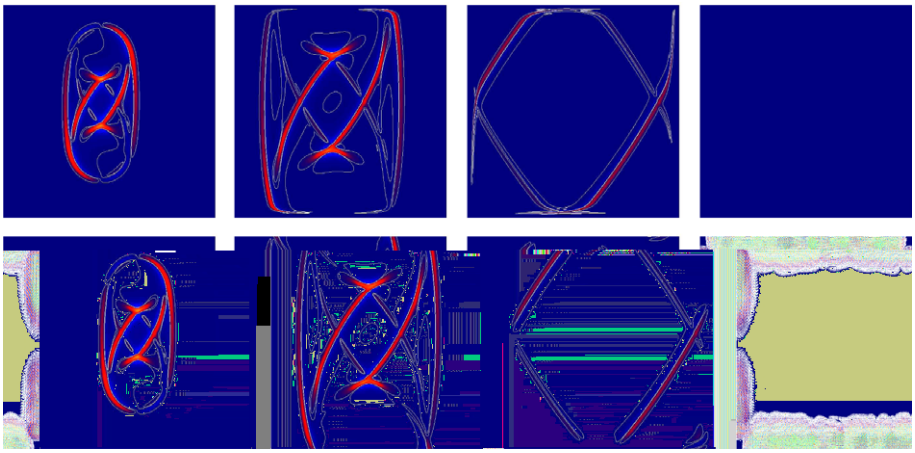

Fig. 13. Top row: The velocity in the x_1 direction is plotted at times 1, 2, 6 and 20, for the damping layer. Bottom row: The velocity in the x_1 direction is plotted at times 1, 2, 6 and 20, for the PML. The color map the ranges from 0.2 (bright red) to -0.2 (light blue). The white contours at -0.001 and 0.001 illustrates that the reflections are small as the waves exit the domain and gets damped in the layers. As can be seen in the last figure, the PML becomes unstable at late times. (For interpretation of the references to colour in this figure legend, the reader is referred to the web version of this article.)

In Fig. 12(b) the rms of $v_i, i = 1, \ldots, 5$, as a function of time for the PML layer and the eight-order super-grid-scale layer are plotted. In the same figure we compare the rms of $v_i, i = 1, \ldots, 5$, for different refinements for the second- and eight-order damping. As for the previous experiments, the high-order damping outperforms the low-order damping and has converged to the true solution on the coarsest grid.

3.3.2. Application to the elastic wave equation in second-order form

For the particular case of an isotropic media the elastic coefficients can be reformulated in terms of the Lamé coefficients $c_{11} = c_{22} = 2\mu + \lambda$, $c_{12} = \lambda$, $c_{33} = \mu$. Eq. (26) then simplifies to

$$\rho \frac{\partial^2 u_1}{\partial t^2} = \frac{\partial}{\partial x_1}\left((2\mu+\lambda)\frac{\partial u_1}{\partial x_1} + \lambda \frac{\partial u_2}{\partial x_2}\right) + \frac{\partial}{\partial x_2}\left(\mu\left(\frac{\partial u_2}{\partial x} + \frac{\partial u}{\partial x_2}\right)\right), \tag{28}$$

$$\rho \frac{\partial^2 u_2}{\partial t^2} = \frac{\partial}{\partial x}\left(\mu\left(\frac{\partial u_2}{\partial x} + \frac{\partial u}{\partial x_2}\right)\right) + \frac{\partial}{\partial x_2}\left(\lambda \frac{\partial u}{\partial x} + (2\mu+\lambda)\frac{\partial u_2}{\partial x_2}\right). \tag{29}$$

We consider the case of an elastic wave guide, unbounded in the x_1 direction. On the top ($x_2 = x_2^{max}$) and bottom ($x_2 = x_2^{min}$) the boundary conditions are either of Dirichlet type

$$u_1(x_1,x_2,t) = u_2(x_1,x_2,t) = 0, \quad x_2 = x_2^{min}, x_2^{max},$$

or traction-free

$$\left(\lambda \frac{\partial u_1(x_1,x_2,t)}{\partial x_1} + (2\mu+\lambda)\frac{\partial u_2(x_1,x_2,t)}{\partial x_2}\right) = 0,$$
$$\mu\left(\frac{\partial u_2(x_1,x_2,t)}{\partial x_1} + \frac{\partial u(x_1,x_2,t)}{\partial x_2}\right) = 0, \quad x_2 = x_2^{min}, \quad x_2^{max}.$$

The stability properties of a perfectly matched layer model for the frequency domain version of the above problem with two free surfaces were recently studied by Skelton et al. in [28]. Skelton et al. showed that some of the surface-to-surface waves, present in elastic wave guides with free surfaces, have oppositely directed phase and group velocities. They found that these backwards propagating waves deteriorate the absorption of their PML. They also suggested that the problem could be remedied by constructing a frequency-dependent PML with a damping whose sign depends on the frequency. As we will se below, the loss in performance in frequency domain translates into the instabilities in the time domain. Unfortunately it is inconvenient to split the waves based on frequency in time domain computations, and it is unclear if it is possible to construct a practically useful and stable PML for such situations.

From an application point of view, the instability discovered in [28] is significant. Not only it is present in many engineering solid-mechanics problems where wave guides are present, but the waves from which it origins also occur in seismological simulations on truncated domains. As we will see below the instability is also present when there is one free and one clamped boundary inside the PML. In addition, in additional experiments (not shown here) it is shown that the same type of instability can occur for stratified media where the internal interfaces act as wave guides and backward propagating trapped modes can be excited. Fortunately the super-grid-scale method generalizes easily to systems in second-order form and may be used as a stable alternative to PML.

3.3.3. Numerical experiments

We demonstrate the instabilities of the PML by solving (28) and (29) in a wave guide $(x_1,x_2) \in (-\infty,\infty)\times[-2,0]$ with traction-free top and bottom. The initial data are a pulse centered at $(x_1,x_2) = (-2,-0.5)$:

$$u_1(x,y,0) = 5(x_1+2)e^{-100((x_1+2)^2+(x_2+0.5)^2)},$$
$$u_2(x,y,0) = 5(x_2+2)e^{-100((x_1+2)^2+(x_2+0.5)^2)}.$$

We truncate the waveguide to the left at $x_1 = -3$ by adding a layer of width 0.4. To the right we truncate at $x_1 = 4$ with Dirichlet conditions for the displacement. The layer is either the PML derived in Appendix B or the damping layer obtained by adding

$$\sigma(x)\frac{\partial^4 \partial u}{\partial x^4 \partial t}, \quad \sigma(x)\frac{\partial^4 \partial v}{\partial x^4 \partial t}, \tag{30}$$

to the right-hand side of (28) and (29). For this example we used an existing curvilinear solver, so rather than slowing down the waves by changing the wave speed we simply applied a smooth stretching of the x_1 coordinate. For the damping layer the equations are discretized as described in [29]. A derivation of the PML and its discretization is found in Appendix B.

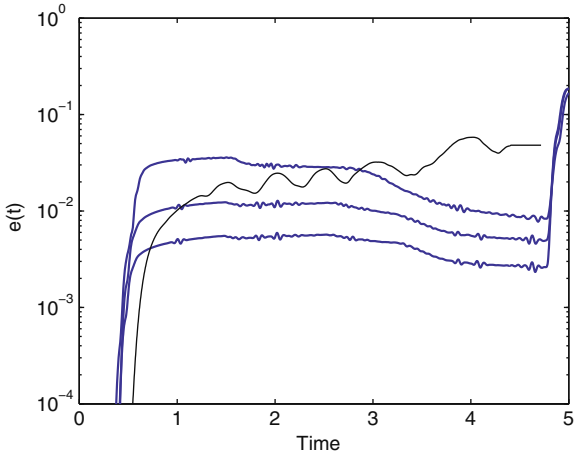

With the above initial data u_1 and u_2 become antisymmetric and symmetric about $x_1 = -2$ and we can measure the error as

$$e(t) = \left(\int_{-2}^{0} \int_{0}^{1} (u_1(-2+x,y) + u_1(-2-x,y))^2 + (u_2(-2+x,y) - u_2(-2-x,y))^2 \, dx dy \right)^{\frac{1}{2}}. \tag{31}$$

In Fig. 14 the relative error (normalized by half of the L_2 norm of the initial data) is plotted as a function of time for the PML and the super-grid layer with free surfaces at the top and bottom. The error in the damping layer is decreased as the grid is refined with a factor between two and four. Compared to the level of the errors in the previous sections the errors here are larger, due to the low-order (second) accurate method used for the computations. For the grid size $h = 0.01$ the relative error is roughly 1% which is about the expected size for the number of points per wavelength (about 40) in the present example. The error for the PML rises somewhat later than for the damping layer, but is increasing rapidly. The increase is not a manifestation of lack of performance of the PML, but rather of the unstable trapped backwards propagating modes.

4. Summary and future work

The application of the super-grid-scale method to linear hyperbolic systems was presented. The reduction of unbounded to bounded domains was performed by smooth coordinate transformations and the damping of super-grid scales was achieved by undivided differences. It was demonstrated by numerical experiments that the reflections caused by the damping are reduced drastically by using high-order undivided differences.

In numerical experiments with Maxwell's equations it was found that the error converges at the order of the numerical method, when high-order damping is used. The levels of the errors are comparable to those obtained with PML.

Two examples for which PML is unstable, the propagation of elastic waves in anisotropic media and in isotropic media with free surface boundary conditions were also considered. It was found that the super-grid-scale method was both accurate and stable for these problems.

We found the presented results encouraging but they can most likely be improved further. Some aspects that warrant further investigation are (some pointed out by the anonymous reviewers):

(i) To optimize the damping for a particular spatial discretization the dispersion relation of that method can be used to tune the viscosity to damp waves with the wrong group velocity. Such tuning will depend on the coordinate transform used.
(ii) In this work the shape of the damping and stretching functions are chosen empirically based on experience and numerical experiments. For a particular spatial discretization it should be possible to find (near) optimal damping and stretching functions.

Acknowledgment

We would like to thank the anonymous reviewers for the constructive comments.

Appendix A. A perfectly matched layer for the elastic wave equation on second-order form

We construct a PML in the x_1-direction for (28) and (29). After Laplace transform in space ($t \to s$) and Fourier transform in the tangential direction ($x_2 \to ik_2$) they become

$$\rho s^2 \hat{u_1} = \frac{d}{dx_1}\left((2\mu+\lambda)\frac{d}{dx_1}\hat{u_1} + \lambda i k_2 \hat{u_2} \right) + i k_2 \left(\mu \left(\frac{d}{dx_1}\hat{u_2} + i k_2 \hat{u_1} \right) \right), \tag{A.1}$$

$$\rho s^2 \hat{u_2} = \frac{d}{dx_1}\left(\mu \left(\frac{d}{dx_1}\hat{u_2} + i k_2 \hat{u_1} \right) \right) + i k_2 \left(\lambda \frac{d}{dx_1}\hat{u_1} + (2\mu+\lambda) i k_2 \hat{u_2} \right). \tag{A.2}$$

Inserting modal solutions $\hat{u}_1 = \hat{\phi}_1 e^{\kappa x_1}$, $\hat{u}_2 = \hat{\phi}_2 e^{\kappa x_1}$ into (A.1) and (A.2), we obtain the eigenvalue problem

$$\rho s^2 \hat{u}_1 = \kappa((2\mu+\lambda)\kappa\hat{u}_1 + \lambda i k_2 \hat{u}_2) + i k_2(\mu(\kappa\hat{u}_2 + i k_2 \hat{u}_1)), \tag{A.3}$$

$$\rho s^2 \hat{u}_2 = \kappa(\mu(\kappa\hat{u}_2 + i k_2 \hat{u}_1)) + i k_2(\lambda\kappa\hat{u}_1 + (2\mu+\lambda) i k_2 \hat{u}_2). \tag{A.4}$$

In the layer we would like the solutions to decay exponentially and thus postulate the modal solution

$$\begin{pmatrix} \hat{u}_1 \\ \hat{u}_2 \end{pmatrix} = \begin{pmatrix} \hat{\phi}_1 \\ \hat{\phi}_2 \end{pmatrix} e^{\kappa x_1 + \frac{\kappa}{s+\alpha}\int_0^{x_1} \sigma(z) dz}. \tag{A.5}$$

Taking d/dx_1 of, for example, the first row of (A.5) we get

$$\kappa\hat{u}_1 = \left(1 - \frac{\sigma(x_1)}{s+\alpha+\sigma}\right)\frac{d}{dx_1}\hat{u}_1. \tag{A.6}$$

To localize in time we introduce the auxiliary variables

$$\hat{\eta}^{(1)} = -\frac{1}{s+\alpha+\sigma(x_1)}\frac{d\hat{u}_1}{dx_1}, \quad \hat{\xi}^{(1)} = -\frac{1}{s+\alpha+\sigma(x_1)}\frac{d\hat{u}_2}{dx_1},$$

and

$$\hat{\eta}^{(2)} = -\frac{1}{s+\alpha+\sigma(x_1)}\left((2\mu+\lambda)\left(\frac{d}{dx_1}\hat{u}_1 + \sigma(x_1)\hat{\eta}^{(1)}\right) + \lambda i k_2 \hat{u}_2\right),$$
$$\hat{\xi}^{(2)} = -\frac{1}{s+\alpha+\sigma(x_1)}\left(\mu\left(\left(\frac{d}{dx_1}\hat{u}_2 + \sigma(x_1)\hat{\xi}^{(1)}\right) + i k_2 \hat{u}_1\right)\right).$$

Inverting the transforms we obtain the following set of equations:

$$\rho\frac{\partial^2 u_1}{\partial t^2} = \frac{\partial}{\partial x}\left((2\mu+\lambda)\left(\frac{\partial u_1}{\partial x} + \sigma\eta^{(1)}\right) + \lambda\frac{\partial u_2}{\partial x_2}\right) + \frac{\partial}{\partial x_2}\left(\mu\left(\frac{\partial u_2}{\partial x} + \sigma\xi^{(1)} + \frac{\partial u_1}{\partial x_2}\right)\right) + \sigma\eta^{(2)}, \tag{A.7}$$

$$\rho\frac{\partial^2 u_2}{\partial t^2} = \frac{\partial}{\partial x_1}\left(\mu\left(\frac{\partial u_2}{\partial x_1} + \sigma\xi^{(1)}\right) + \mu\frac{\partial u_1}{\partial x_2}\right) + \frac{\partial}{\partial x_2}\left(\lambda\left(\frac{\partial u_1}{\partial x_1} + \sigma\eta^{(1)}\right) + (2\mu+\lambda)\frac{\partial u_2}{\partial x_2}\right) + \sigma\xi^{(2)}, \tag{A.8}$$

$$\frac{\partial\eta^{(1)}}{\partial t} + (\alpha+\sigma)\eta^{(1)} = -\frac{\partial u_1}{\partial x_1}, \tag{A.9}$$

$$\frac{\partial\xi^{(1)}}{\partial t} + (\alpha+\sigma)\xi^{(1)} = -\frac{\partial u_2}{\partial x_1}, \tag{A.10}$$

$$\frac{\partial\eta^{(2)}}{\partial t} + (\alpha+\sigma)\eta^{(2)} = -\frac{\partial}{\partial x_1}\left((2\mu+\lambda)\left(\frac{\partial u_1}{\partial x_1} + \sigma\eta^{(1)}\right) + \lambda\frac{\partial u_2}{\partial x_2}\right), \tag{A.11}$$

$$\frac{\partial\xi^{(2)}}{\partial t} + (\alpha+\sigma)\xi^{(2)} = -\frac{\partial}{\partial x_1}\left(\mu\left(\frac{\partial u_2}{\partial x_1} + \sigma\xi^{(1)}\right) + \mu\frac{\partial u_1}{\partial x_2}\right). \tag{A.12}$$

A.1. Discretization

Discretization of the above equations is based on the one described in [29]. The spatial derivatives in (A.9) and (A.10) are discretized by second-order accurate centered-finite difference approximations. The time derivatives in new Eqs. (A.9)–(A.12) are discretized by the second-order Adams–Bashforth method.

Appendix B. The perfectly matched layer used in Section 3.2.1

The perfectly matched layer used in Section 3.2.3 is:

$$\begin{aligned}
&\frac{\partial E_z}{\partial t} = \eta\left(\frac{\partial H_y}{\partial x} + \gamma\sigma\phi^{(2)}\right) - \frac{\partial H_x}{\partial y},\\
&\frac{\partial H_x}{\partial t} = -\frac{\partial E_z}{\partial y},\\
&\frac{\partial H_y}{\partial t} = \eta\left(\frac{\partial E_z}{\partial x} + \gamma\sigma\phi^{(1)}\right),\\
&\frac{\partial\phi^{(1)}}{\partial t} + \gamma\sigma\phi^{(1)} = -\frac{\partial E_z}{\partial x},\\
&\frac{\partial\phi^{(2)}}{\partial t} + \gamma\sigma\phi^{(2)} = -\frac{\partial H_y}{\partial x}.
\end{aligned} \tag{B.1}$$

In the presented computations we use $\gamma = 30$, and σ determined by (25) with $p = 3$, $q = 4$.

References

[1] T. Colonius, H. Ran, A super-grid-scale model for simulating compressible flow on unbounded domains, Journal of Computational Physics 182 (1) (2002) 191–212.

[2] T. Hagstrom, S. Lau, Radiation boundary conditions for Maxwell's equations: a review of accurate time-domain formulations, Journal of Computational Mathematics 25 (2007) 305–336.
[3] T. Colonius, Modeling artificial boundary conditions for compressible flow, Annual Review of Fluid Mechanics 36 (2004) 315–345.
[4] T. Hagstrom, New results on absorbing layers and radiation boundary conditions, in: Ch.T. Hagstrom (Ed.), Topics in Computational Wave Propagation, in: M. Ainsworth, P. Davies, D. Duncan, P. Martin, B. Rynne (Eds.), Lecture Notes in Computational Science and Engineering, vol. 31, Springer-Verlag, New York, 2003, pp. 1–42.
[5] D. Givoli, High-order local non-reflecting boundary conditions: a review, wave motion, New Computational Methods for Wave Propagation 39 (2004) 319–326.
[6] T. Hagstrom, T. Warburton, High-order local radiation boundary conditions: corner compatibility conditions and extensions to first order systems, Wave Motion 39 (2004) 327–338.
[7] J. Bérenger, A perfectly matched layer for the absorption of electromagnetic waves, Journal of Computational Physics 114 (1994) 185.
[8] E. Bécache, S. Fauqueux, P. Joly, Stability of perfectly matched layers group,velocities and anisotropic waves, Journal of Computational Physics 188 (2003) 399–433.
[9] C. Grosch, S. Orszag, Numerical-solution of problems in unbounded regions – coordinate transforms, Journal of Computational Physics 25 (3) (1977) 273–295.
[10] M. Israeli, S. Orzag, Approximation of radiation boundary conditions, Journal of Computational Physics 41 (1981) 115–135.
[11] R. Kosloff, D. Kosloff, Absorbing boundaries for wave-propagation problems, Journal of Computational Physics 63 (1986) 363–376.
[12] S. Karni, Far-field filtering operators for supression of reflections of artificial boundaries, SIAM Journal on Numerical Analysis 33 (1996) 1014–1047.
[13] M. Visbal, D. Gaitonde, Very high-order spatially implicit schemes for computational acoustics on curvilinear meshes, Journal of Computational Acoustics 9 (4) (2001) 1259–1286.
[14] M. White, M. Visbal, Using filters to design absorbing boundary conditions for high-order CEM, IEEE Transactions on Magnetics (March) (2004).
[15] L. Trefethen, Group-velocity in finite-difference schemes, SIAM Review 24 (1982) 113–136.
[16] R. Vichnevetsky, Invariance theorems concerning reflection at numerical boundaries, Journal of Computational Physics 63 (1986) 268–282.
[17] R. Vichnevetsky, Wave-propagation analysis of difference-schemes for hyperbolic-equations – a review, International Journal For Numerical Methods in Fluids 7 (5) (1987) 409–452.
[18] T. Colonius, S. Lele, Computational aeroacoustics: progress on nonlinear problems of sound generation, Progress in Aerospace Sciences 40 (2004) 345–416.
[19] K. Mattsson, J. Nordstrom, Summation by parts operators for finite difference approximations of second derivatives, Journal of Computational Physics 199 (2004) 503–540.
[20] B. Gustafsson, H. Kreiss, J. Oliger, Time Dependent Problems and Difference Methods, Pure and Applied Mathematics, Wiley, New York, 1995.
[21] H. Kreiss, J. Lorenz, Initial-boundary Value Problems and The Navier–Stokes Equations, Pure and Applied Mathematics, vol. 136, Academic Press, Boston, 1989.
[22] G. Bres, T. Colonius, Interaction of acoustic disturbances with micro-cavities for ultrasonic absorptive coatings, in: 5th AIAA Theoretical Fluid Mechanics Conference Seattle, Washington, June 23–26, 2008, No. AIAA 2008-3903, 2008.
[23] P. Olsson, The numerical behavior of high-order finite difference methods, Journal of Scientific Computing 9 (4) (1994) 445–466.
[24] T. Hagstrom, J. Goodrich, Experiments with approximate radiation boundary conditions for computational aeroacoustics, Applied Numerical Mathematics 27 (4) (1998) 385–402.
[25] B. Alpert, L. Greengard, T. Hagstrom, Nonreflecting boundary conditions for the time-dependent wave equation, Journal of Computational Physics 180 (1) (2002) 270–296.
[26] C. Tsitouras, S.N. Papakostas, Cheap error estimation for Runge–Kutta methods, SIAM Journal on Scientific Computing 20 (1999) 2067–2088.
[27] D. Appelö, G. Kreiss, A new absorbing layer for elastic waves, Journal of Computational Physics 215 (2) (2006) 642–660.
[28] E.A. Skelton, S.D.M. Adams, R.V. Craster, Guided elastic waves and perfectly matched layers, Wave Motion 44 (7) (2007) 573–592.
[29] D. Appelö, N.A. Petersson, A stable finite difference method for the elastic wave equation on complex geometries with free surfaces, Communications in Computational Physics 5 (1) (2009) 84–107.